Letter
Vol. 50, No. 4 / 15 February 2025 / Optics Letters 1253

Optics Letters

Robust multimode interference and conversion in topological unidirectional surface magnetoplasmons

Chao Liu,[1,2] Ziyang Zhao,[2] Tianjing Guo,[2] Jie Xu,[3] Xiaohua Deng,[2] Kai Yuan,[1] Rongxin Tang,[2] Kosmas L. Tsakmakidis,[4,5] and Lujun Hong[1,2,*]

[1]School of Information Engineering, Nanchang University, Nanchang 330031, China
[2]Institute of Space Science and Technology, Nanchang University, Nanchang 330031, China
[3]School of Medical Information and Engineering, Southwest Medical University, Luzhou 646000, China
[4]Section of Condensed Matter Physics, Department of Physics, National and Kapodistrian University of Athens Panepistimiopolis, Athens GR-157 84, Greece
[5]ktsakmakidis@phys.uoa.gr
*ljhong@ncu.edu.cn

Received 6 September 2024; revised 19 January 2025; accepted 19 January 2025; posted 22 January 2025; published 10 February 2025

We have theoretically investigated surface magnetoplasmons (SMPs) in an yttrium-iron-garnet (YIG) sandwiched waveguide. The dispersion demonstrated that this waveguide can support topological unidirectional SMPs. Based on unidirectional SMPs, magnetically controllable multimode interference (MMI) is verified in both symmetric and asymmetric waveguides. Due to the coupling between the modes along two YIG–air interfaces, the asymmetric waveguide supports a unidirectional even mode within a single-mode frequency range. Moreover, these modes are topologically protected when a disorder is introduced. Utilizing robust unidirectional SMP MMI (USMMI), tunable splitters have been achieved. It has been demonstrated that mode conversion between different modes can be realized. These results provide many degrees of freedom to manipulate topological waves.

https://doi.org/10.1364/OL.541177

Topological unidirectional waves have attracted much attention due to their unique optical properties of wave propagation protected from backscattering [1–4]. As analogs of quantum Hall edge states in photonic crystals (PhCs) [5], unidirectional edge modes were proven in yttrium-iron-garnet (YIG) PhCs [6], and they were first experimentally observed at microwave frequencies [7]. Due to the time-reversal symmetry broken by an external magnetic field (EMF), such modes can travel in only one direction and are robust against backscattering from a disorder [8,9]. As another type of unidirectional mode, surface magnetoplasmons (SMPs) were also proposed [10,11], attracting great interest due to the rich physics of nonreciprocal and topological materials [12–15]. Recently, topologically unidirectional SMP propagation was experimentally verified in a YIG-based SMP waveguide [16].

Owing to their nontrivial topologically protected properties [17,18], unidirectional modes based on PhCs or SMPs are suitable for realizing topologically optical devices, such as logic gates [19], lasers [20], slow light [21], and splitters [22,23]. Recently, multimode interference (MMI) was achieved using topological PhCs, demonstrating robustness against a disorder [24,25]. Mode conversion has also been realized in a YIG-based PhC waveguide [26]. More recently, magnetically controllable MMI based on topological YIG PhCs was demonstrated [27]. It is a natural desire to investigate whether an SMP waveguide can achieve MMI and mode conversion. In this Letter, we will show that magnetically controllable unidirectional SMP MMI (USMMI) can be achieved. Based on such USMMI, tunable splitters are designed in symmetric and asymmetric structures, demonstrating robustness against a disorder. Notably, a unidirectional even mode occurs within a single-mode frequency range in the asymmetric waveguide, unlike in conventional SMP waveguides. This finding enables us to achieve efficient mode conversion through the coupling of different waveguides.

We consider a waveguide composed of two YIG slabs sandwiched between a metal and dielectric, as shown in Fig. 1(a). The dielectric layer with thickness h has a permittivity of ε_r. The two YIG slabs with thickness d are magnetized by two opposing EMFs (H_1 and H_2), along the $\pm z$ direction. Owing to the EMFs, the YIG slabs are gyromagnetically anisotropic with a relative permittivity of $\varepsilon_m = 15$ and permeability tensor μ_m [28,29]:

$$\mu_m^+ = \begin{bmatrix} \mu_1 & -i\mu_2 & 0 \\ i\mu_2 & \mu_1 & 0 \\ 0 & 0 & 1 \end{bmatrix}, \quad \mu_m^- = \begin{bmatrix} \mu_1' & i\mu_2' & 0 \\ -i\mu_2' & \mu_1' & 0 \\ 0 & 0 & 1 \end{bmatrix} \tag{1}$$

with $\mu_1 = 1 + \frac{\omega_m(\omega_0+i\alpha\omega)}{(\omega_0+i\alpha\omega)^2-\omega^2}$, $\mu_2 = \frac{\omega_m\omega}{(\omega_0+i\alpha\omega)^2-\omega^2}$, $\mu_1' = 1+\frac{\omega_m(\omega_0'+i\alpha\omega)}{(\omega_0'+i\alpha\omega)^2-\omega^2}$, and $\mu_2' = \frac{\omega_m\omega}{(\omega_0'+i\alpha\omega)^2-\omega^2}$, where $\omega_0 = 2\pi\gamma H_1$, $\omega_0' = 2\pi\gamma H_2$ ($\gamma = 2.8$ MHz/G is the gyromagnetic ratio) is the resonance frequency, ω is the angular frequency, α is the damping coefficient, and ω_m is the characteristic circular frequency. This waveguide can support the transverse electric (TE) mode (H_x, H_y, E_z). By solving Maxwell's equations with the continuous boundary conditions, the dispersion relation of SMPs can be derived analytically as follows (see the details

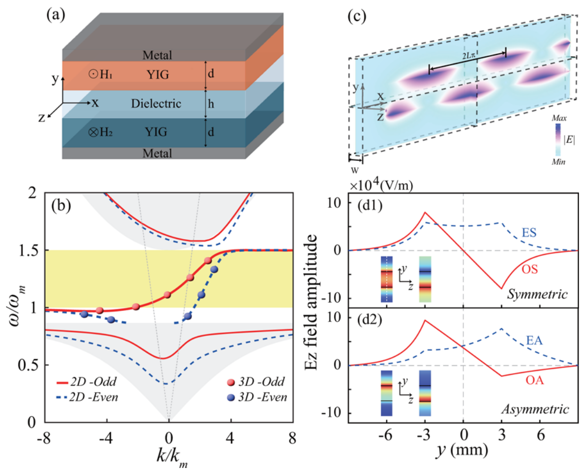

Fig. 1. (a) Schematic of the proposed topological waveguide with opposing EMFs in two YIG slabs. (b) Dispersion relation of the odd mode (solid lines) and even mode (dashed lines) in the 2D symmetric structure. Circles indicate results for the 3D realistic system. The unidirectional propagation occurs in $[\omega_m, 1.5\omega_m]$, marked by yellow. The gray shaded area represents the YIG bulk modes. (c) Simulated E-field amplitude at $\omega = 1.1\omega_m$ in the 3D waveguide. Distribution of the E_z field along the y axis in symmetric (d1) and asymmetric (d2) structures. Insets show the mode profiles. The parameters are $d = 0.1\lambda_m$, $h = 0.1\lambda_m$, $W = 0.05\lambda_m$, and $H_1 = H_2 = 893$ G.

Supplement 1):

$$e^{2\alpha_r h} = \frac{\left(1 - \frac{M}{\alpha_r \mu_v}\right)\left(1 - \frac{N}{\alpha_r \mu_v'}\right)}{\left(1 + \frac{M}{\alpha_r \mu_v}\right)\left(1 + \frac{N}{\alpha_r \mu_v'}\right)}, \quad (2)$$

with $M = k\frac{\mu_2}{\mu_1} + \frac{\alpha_1}{\tanh \alpha_1 d}$ and $N = k\frac{\mu_2'}{\mu_1'} + \frac{\alpha_2}{\tanh \alpha_2 d}$, where k is the propagation constant and $\alpha_r = \sqrt{k^2 - \epsilon_r k_0^2}$ ($k_0 = \omega/c$ is the vacuum wavenumber), $\alpha_1 = \sqrt{k^2 - \mu_v \epsilon_m k_0^2}$, and $\alpha_2 = \sqrt{k^2 - \mu_v' \epsilon_m k_0^2}$ ($\mu_v = \mu_1 - \mu_2^2/\mu_1$ and $\mu_v' = \mu_1' - {\mu_2'}^2/\mu_1'$ are the Voigt permeabilities) are the attenuation coefficients in the dielectric, upper, and lower YIG slabs, respectively. It is found from Eq. (2) that SMPs have four asymptotic frequencies when $k \to \pm\infty$: $\omega_{sp1} = \omega_0 + 0.5\omega_m$, $\omega_{sp2} = \omega_0 + \omega_m$, $\omega_{sp3} = \omega_0' + 0.5\omega_m$, and $\omega_{sp4} = \omega_0' + \omega_m$. In the special case of $H_1 = H_2$, the dispersion relation of SMPs in Eq. (2) can be simplified to the following:

$$k\frac{\mu_2}{\mu_1} + \frac{\alpha_1}{\tanh \alpha_1 d} + \alpha_r \mu_v \tanh\left(\frac{\alpha_r h}{2}\right) = 0 \quad (ES) \quad (3a)$$

$$k\frac{\mu_2}{\mu_1} + \frac{\alpha_1}{\tanh \alpha_1 d} + \alpha_r \mu_v \coth\left(\frac{\alpha_r h}{2}\right) = 0 \quad (OS), \quad (3b)$$

for the even-symmetric (ES) and odd-symmetric (OS) modes, respectively. The presence of the linear term k in Eq. (3a) leads to different dispersion for forward and backward propagation, resulting in non-reciprocity.

First, we consider a symmetric structure ($H_1 = H_2$). The dispersion of SMPs in this waveguide can be numerically calculated using Eq. (3a). Here, we take $d = 0.1\lambda_m$ ($\lambda_m = 2\pi c/\omega_m$), and $\omega_m = 10\pi \times 10^9$ rad/s for YIG [16], and use air as an example for the dielectric with $\epsilon_r = 1$ and $h = 0.1\lambda_m$. Figure 1(b) shows the dispersion diagram for $H_1 = H_2 = 893$ G, which is equivalent to $\omega_0 = \omega_0' = 0.5\omega_m$. Due to the coupling between SMPs along the two YIG–air interfaces, two nonreciprocal modes (OS and ES) emerge, denoted by the solid and dashed lines. Clearly, a topological unidirectional propagation band occurs in $[\omega_{sp1}, \omega_{sp2}]$, corresponding to $[\omega_m, 1.5\omega_m]$, as marked by the yellow shaded area. The dashed lines represent light line with $\omega = \pm kc$. Such unidirectional modes in the bandgap of the YIG bulk modes with $k^2 < \mu_v \epsilon_m k_0^2$ (the gray shaded areas) are topologically protected due to the nontrivial bandgap [21,30]. Moreover, the 2D structure can be accurately extended to a realistic 3D structure with a waveguide width W, truncated by two metal slabs along the z direction. To illustrate this, we also numerically solve the modes for the realistic 3D system with modal analysis using COMSOL Multiphysics in Fig. 1(b), and the obtained results for $W = 0.05\lambda_m$ (see circles) are in good agreement with those for the 2D system. When both the unidirectional ES and OS modes are excited in the same waveguide, USMMI will occur. To verify this, we simulate the wave propagation in the 3D waveguide shown in Fig. 1(c). A line current source with $\omega = 1.1\omega_m$ is placed at the bottom of the air layer to excite the two unidirectional modes. As expected, the excited wave can only propagate in one direction without any backscattering. Importantly, USMMI with periodic fields of OS and ES is achieved, which can be characterized by the beat length L_π [31]:

$$L_\pi = \frac{\pi}{|k_{odd} - k_{even}|}, \quad (4)$$

where k_{odd} and k_{even} are the propagation constants of the odd and even modes, respectively. Figure 1(d1) shows the corresponding mode profiles (see the inset) and E_z distributions along the y axis for the OS and ES modes in the 3D system, demonstrating their symmetric features. It should be noted that our interest in this work focuses on the unidirectional region.

MMI based on PhCs is useful for designing a tunable splitter [27,32], and either nonlinear mechanisms [33] or, as here, SMP-based MMI can be employed for the same purpose. To verify this, a tunable splitter based on the SMP waveguide is proposed in Fig. 2(a). The input waveguide supports USMMI, while the output waveguide supports a single-mode SMP, whose dispersion relation in the metal–YIG–air–metal structure is the

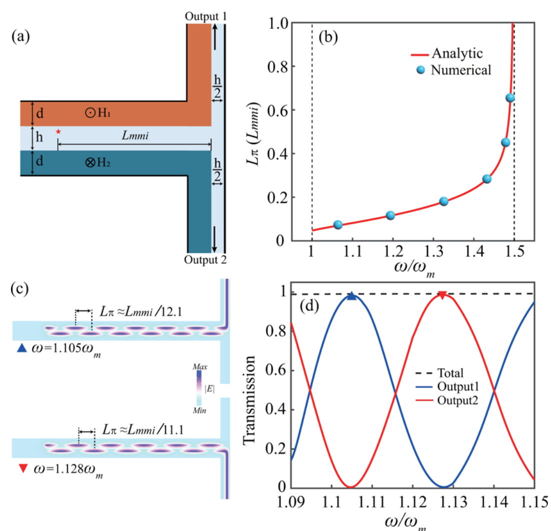

Fig. 2. (a) Schematic of the splitter based on USMMI. (b) Analytical (solid line) and numerical (circles) results of beat length L_π as a function of ω. (c) Simulated E-field amplitudes in the symmetric splitter at $\omega = 1.105\omega_m$ and $1.128\omega_m$. (d) Transmission coefficients of the symmetric splitter ($H_1 = H_2 = 893$ G) as a function of ω.

same as that of the OS mode in Eq. (3b) [14,16]. The point source is placed at a distance of L_{mmi} (the length of the MMI) from the junction. For USMMI, the inverted and direct images of the input field periodically alternate with a constant L_π, as shown in Fig. 1(c). Figure 2(b) shows the analytic beat length L_π using Eq. (4) as a function of ω, indicated by the red solid line. It can be seen that L_π increases with ω across the entire USMMI region. Moreover, we calculate the numerical values of L_π by full-wave simulations for various frequencies, as shown by the circles in Fig. 2(b), which agree well with the analytical values. To verify the tunability of the splitter, the transmission coefficients of the symmetric splitter ($H_1 = H_2 = 893$ G) as a function of ω are shown in Fig. 2(d). Here, we take the loss with $\alpha=3\times10^{-5}$ as an example (for the impact of loss, see Supplement 1). As ω changes from $1.09\omega_m$ to $1.15\omega_m$, the transmission of each output oscillates between nearly 0 and 1. The total transmission is always 1 for lossless ($\alpha = 0$) due to the topological unidirectional feature. To clearly illustrate this, the simulated E-field amplitudes of the splitter at $\omega = 1.105\omega_m$ and $1.128\omega_m$ are displayed in Fig. 2(c). The value of L_{mmi} satisfies as $L_{mmi} \approx 12.1L_{\pi(1.105\omega_p)} \approx 11.1L_{\pi(1.128\omega_p)}$, with an inverted (direct) image of the incident field are realized at the upper (lower) corner. Consequently, the unidirectional SMP propagates upward (downward) along Output1 (Output2) at frequencies of 1.105 ω_m (1.128 ω_m) as expected. The results demonstrate that a frequency splitter based on USMMI is achieved. It should be noted that a magnetically controllable power splitter (see Supplement 1) can also be realized using USMMI.

Second, we analyze an asymmetric structure ($H_1 \neq H_2$). Here, we take $H_1 = 893$ G and $H_2 = 300$ G as an example, with other parameters being the same as in Fig. (1). Using Eq. (2), we numerically calculate the dispersion relation of SMPs for the asymmetric waveguide. Figure 3(a) displays the dispersion diagram for $d = 0.1\lambda_m$. Due to the asymmetric coupling between modes along the two YIG–air interfaces, the waveguide supports four modes: EA, OA, S1, and S2 modes. The EA and OA mode

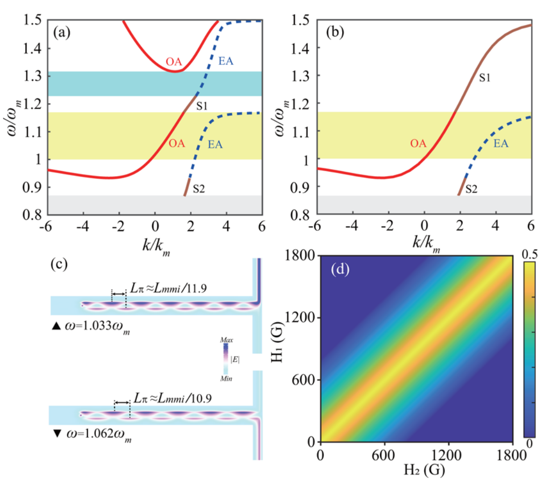

Fig. 3. (a) and (b) Dispersion relation of SMPs in an asymmetric waveguide for $H_1 = 893$ G and $H_2 = 300$ G. (a) $d = 0.1\lambda_m$ and (b) $d = 0.05\lambda_m$. The yellow shaded area represents the region of USMMI between the OA and EA double modes, while the bluish shaded area represents the unidirectional EA single mode. S1 and S2 represent the single modes supported at the YIG–air surfaces. (c) Simulated E-field amplitudes in the asymmetric splitter at $\omega = 1.033\omega_m$ and $1.062\omega_m$. (d) USMMI bandwidth $\Delta\omega$ as a function of H_1 and H_2.

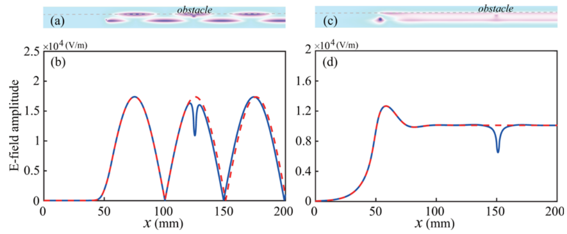

Fig. 4. (a) and (c) Simulated E-field amplitudes in symmetric (a) and asymmetric (c) structures. (b) and (d) Distributions of E-field amplitudes in (a) and (c) along the upper YIG–air interface (gray dashed lines), respectively. The blue solid and red dashed lines represent the results with and without the obstacles, respectively. The operating frequency is $\omega = 1.28\omega_m$.

profiles at $\omega = 1.1\omega_m$ are illustrated in Fig. 1(d2), exhibiting even-asymmetric (EA) and odd-asymmetric (OA) characteristics, respectively. The S1 and S2 modes can only propagate at a single surface of the upper or lower YIG–air interface. As shown in Fig. 3(a), there is also a USMMI band (yellow shaded area) for the EA and OA modes in $[\omega_{sp1}, \omega_{sp4}]$, where $\omega_{sp1} = \omega_m$ and $\omega_{sp4} = 1.168\omega_m$. More importantly, there is a bandwidth of $[1.228\omega_m, 1.315\omega_m]$ that supports only a single unidirectional EA mode, which differs from the symmetric waveguide shown in Fig. 1(b). The existence of such a single EA mode is due to the strong coupling between the S1 mode and the higher-order EA modes. Figure 3(b) shows the dispersion diagram for $d = 0.05\lambda_m$. It is found that the band of the single EA mode is significantly affected by the YIG thickness d and disappears when d decreases from $0.1\lambda_m$ to $0.05\lambda_m$. Figure 3(c) shows the simulated E-field amplitudes in the asymmetric splitter at $\omega = 1.033\omega_m$ and $1.062\omega_m$. Similar to the symmetric splitter, the distance L_{mmi} satisfies $L_{mmi} \approx 11.9L_{\pi(1.033\omega_m)} \approx 10.9L_{\pi(1.062\omega_m)}$; thus, the SMP propagates upward and downward as expected. Moreover, the USMMI bandwidth is not affected by d but is only related to H_1 and H_2, resulting from the magnetically controllable asymptotic frequency ω_{sp}. Figure 3(d) shows the USMMI bandwidth versus the magnetic fields H_1 and H_2, defined by $\Delta\omega = \max\left(0.5\omega_m - \frac{|H_1-H_2|}{1786}\omega_m, 0\right)$. It can be seen that the bandwidth $\Delta\omega$ is magnetically controllable by varying H_1 and H_2, and reaching a maximum value of $0.5\omega_m$ when $H_1 = H_2$.

Due to the topological protection of the unidirectional mode [18], our proposed SMP waveguides are robust against a disorder. To verify this robustness, two 1 mm square YIG obstacles were introduced into the air layer of both the symmetric [Fig. (1)] and asymmetric [Fig. (3)] waveguides. Figures 4(a) and 4(c) show the simulated results of full-wave simulations at $\omega = 1.28\omega_m$, respectively. As seen in Fig. 4(a), the pattern of USMMI in the symmetric waveguide remains almost constant before and after the obstacle. Similarly, it is invariant in the asymmetric waveguide. More importantly, it is found from Fig. 4(c) that the newly emerged unidirectional EA mode effectively circumvents the obstacle without any backscattering, clearly demonstrating its unidirectional dispersion property in Fig. 3(a). Figures 4(b) and 4(d) show the distributions of E-field amplitudes along the upper YIG–air interface, corresponding the gray dashed lines in Fig. 4. For comparison, the results without defects are also shown by the red dashed lines. The field amplitudes closely resemble those with obstacles (blue solid lines), demonstrating the strong robustness of the SMP modes in our proposed symmetric and asymmetric systems.

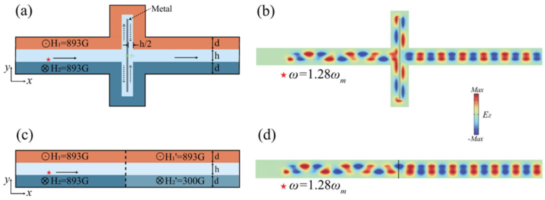

Fig. 5. Structure of mode conversion with (a) and without (c) additional metal plate. (b) and (d) Simulated E_z field amplitudes in the symmetric (a) and asymmetric (c) structures, demonstrating that the unidirectional multiple modes are transferred to a single even mode. The stars mark the source with $\omega = 1.28\omega_m$, and the dashed lines in (c) and (d) represent the boundaries between distinct waveguides.

Finally, we demonstrate the capability of mode conversion between different modes. For this purpose, two different types of mode conversion are considered. The first involves by inserting a metal plate into the waveguide, analogous to the combination of two splitters, as shown in Fig. 5(a). In this waveguide, an excited wave is equally split into two waves, with the difference of initial phase $\Delta\phi_0$ and displacement Δl, and then they coupled to a wave. Mode conversion occurs only when $k\Delta l + \Delta\phi_0 = n\pi$, where $\Delta l = 4y_c$, and y_c is the center position of the metal plate along the y axis. The metal is assumed to be a perfect electric conductor (PEC) with a length of $1.4\lambda_m$. By appropriately adjusting y_c, the incident mode can be converted to an even mode when $n = 0, \pm 2, \pm 4 \ldots$ and to odd modes when $n = \pm 1, \pm 3, \pm 5 \ldots$. Figure 5(b) shows the simulated E_z field pattern for $\omega = 1.28\omega_m$. It is found that the conversion between multiple modes and the even mode can be achieved, when $y_c = -0.036\lambda_m$. Furthermore, the conversion between the even and odd modes can also be realized by varying y_c in this waveguide. More importantly, the second type of mode conversion, without additional metal plate to change the wave phase, is proposed by connecting the two waveguides shown in Fig. 5(c). In this structure, the left part is a symmetric waveguide [Fig. 4(a)], while the right part is an asymmetric waveguide [Fig. 4(b)]. Figure 5(d) shows the simulated E_z field pattern for $\omega = 1.28\omega_m$. Since only one even mode exists in the right waveguide at this frequency, the excited multiple modes are converted into a single even mode as expected, possessing the advantages of the simple mode conversion structure. Therefore, we conclude that mode conversion, both with and without the insertion of a metal, can be achieved.

In conclusion, we have proposed a waveguide composed of two YIG slabs sandwiched between metal and dielectric layers, which supports multiple SMP modes. The dispersion properties of these SMPs have been analyzed, exhibiting a unidirectional feature. We demonstrated that robust USMMI can be achieved in SMP waveguides, overcoming the limitation of backscattering in traditional waveguides. Furthermore, tunable splitters based on USMMI have been designed in both symmetric and asymmetric structures. USMMI has been shown to be immune to disorders, and mode conversion can also be realized. Notably, the asymmetric waveguide supports only an even mode within a specific single-mode frequency range, differing from the behavior observed in a symmetric waveguide. These results can be extended to terahertz and optical frequencies, offering significant flexibility to manipulate topological waves.

Funding. National Natural Science Foundation of China (12464057, 12104203); Natural Science Foundation of Jiangxi Province (20224BAB 211015, 20242BAB25039).

Disclosures. The authors declare no conflicts of interest.

Data availability. The data supporting the findings of this study are available from the corresponding author upon reasonable request.

Supplemental document. See Supplement 1 for supporting content.

REFERENCES

1. L. Lu, J. D. Joannopoulos, and M. Soljačić, Nat. Photonics **8**, 821 (2014).
2. X. Cheng, C. Jouvaud, X. Ni, *et al.*, Nat. Mater. **15**, 542 (2016).
3. T. Ozawa, H. M. Price, A. Amo, *et al.*, Rev. Mod. Phys. **91**, 015006 (2019).
4. J. Chen and Z.-Y. Li, Phys. Rev. Lett. **128**, 257401 (2022).
5. F. D. M. Haldane and S. Raghu, Phys. Rev. Lett. **100**, 013904 (2008).
6. Z. Wang, Y. D. Chong, J. D. Joannopoulos, *et al.*, Phys. Rev. Lett. **100**, 013905 (2008).
7. Z. Wang, Y. Chong, J. D. Joannopoulos, *et al.*, Nature **461**, 772 (2009).
8. M. Wang, R.-Y. Zhang, L. Zhang, *et al.*, Phys. Rev. Lett. **126**, 067401 (2021).
9. Y. Poo, R.-x. Wu, Z. Lin, *et al.*, Phys. Rev. Lett. **106**, 093903 (2011).
10. Z. Yu, G. Veronis, Z. Wang, *et al.*, Phys. Rev. Lett. **100**, 023902 (2008).
11. W. Gao, B. Yang, M. Lawrence, *et al.*, Nat. Commun. **7**, 12435 (2016).
12. D. Jin, T. Christensen, M. Soljačić, *et al.*, Phys. Rev. Lett. **118**, 245301 (2017).
13. K. L. Tsakmakidis, L. Shen, S. A. Schulz, *et al.*, Science **356**, 1260 (2017).
14. L. Hong, Y. Wang, Y. Shen, *et al.*, Opt. Mater. Express **11**, 2975 (2021).
15. Y. Liang, S. Pakniyat, Y. Xiang, *et al.*, Optica **8**, 952 (2021).
16. S. Li, K. L. Tsakmakidis, T. Jiang, *et al.*, Nat. Commun. **15**, 5992 (2024).
17. X. Xi, B. Yan, L. Yang, *et al.*, Nat. Commun. **14**, 1991 (2023).
18. D. Jin, L. Lu, Z. Wang, *et al.*, Nat. Commun. **7**, 13486 (2016).
19. J. Xu, Y. Luo, S. Xiao, *et al.*, Adv. Opt. Mater. **11**, 2201836 (2023).
20. B. Bahari, A. Ndao, F. Vallini, *et al.*, Science **358**, 636 (2017).
21. S. A. Mann and A. Alù, Phys. Rev. Lett. **127**, 123601 (2021).
22. D. C. Tee, N. Tamchek, Y. G. Shee, *et al.*, Opt. Express **22**, 24241 (2014).
23. Y. Chen, X.-T. He, Y.-J. Cheng, *et al.*, Phys. Rev. Lett. **126**, 230503 (2021).
24. L. Liu, Y. Wang, F. Zheng, *et al.*, Opt. Lett. **47**, 2634 (2022).
25. L. Liu and Y. Wang, Opt. Laser Technol. **161**, 109224 (2023).
26. Y. Huang, G. Tang, Z.-Y. Li, *et al.*, Opt. Lett. **48**, 4536 (2023).
27. W. Tang, M. Wang, S. Ma, *et al.*, Light: Sci. Appl. **13**, 112 (2024).
28. Y.-T. Fang, P. Gong, and F. Bu, Opt. Laser Technol. **171**, 110309 (2024).
29. F. Chen, H. Xue, Y. Pan, *et al.*, Phys. Rev. Lett. **132**, 156602 (2024).
30. L. Lu, H. Gao, and Z. Wang, Nat. Commun. **9**, 5384 (2018).
31. L. Soldano and E. Pennings, J. Lightwave Technol. **13**, 615 (1995).
32. S. A. Skirlo, L. Lu, and M. Soljacic, Phys. Rev. Lett. **113**, 113904 (2014).
33. P. A. Pantazopoulos, K. L. Tsakmakidis, E. Almpanis, *et al.*, New J. Phys. **21**, 095001 (2019).